Laser & Photonics Reviews

LASER & PHOTONICS REVIEWS

www.lpr-journal.org

RESEARCH ARTICLE OPEN ACCESS

Amplification of Light-Ultrasound Interaction in a Pi-Shifted Fiber Bragg Grating for Enhanced Ultrasonic Sensitivity

Tai-Anh La[1,2] | Rami Shnaiderman[1,2] | Vasilis Ntziachristos[1,2,3]

[1]Chair of Biological Imaging, Central Institute for Translational Cancer Research (TranslaTUM), School of Medicine and Health & School of Computation, Information and Technology, Technical University of Munich, Munich, Germany | [2]Institute of Biological and Medical Imaging, Bioengineering Center, Helmholtz Zentrum München, Neuherberg, Germany | [3]Munich Institute of Biomedical Engineering (MIBE), Technical University of Munich, Garching b. München, Germany

Correspondence: Vasilis Ntziachristos (bioimaging.translatum@tum.de)

Received: 30 April 2025 | **Revised:** 18 September 2025 | **Accepted:** 20 November 2025

Keywords: high Q-factor | optical resonator | optoacoustic | photoacoustic | ultrasound detector

ABSTRACT

Optical resonators offer a promising alternative to conventional piezoelectric transducers in ultrasound detection because they can be miniaturized without a decrease in sensitivity. However, optical-resonator-based detectors still possess a significant sensitivity disadvantage compared to millimeter-scale piezoelectric transducers, preventing the dissemination of these micro-detectors. In this manuscript, we present a new detector design that bridges the sensitivity gap between optical-resonator-based detectors and piezoelectric transducers by amplifying light-ultrasound interaction in a pi-shifted Fiber Bragg grating. The proposed detector has a noise equivalent pressure density <0.5 mPa/$\sqrt{\text{Hz}}$, an ultra-broad bandwidth of more than 100 MHz. We perform a side-by-side comparison between our detector and state-of-the-art piezoelectric bulky transducers employed in pre-clinical optoacoustic systems, revealing comparable performance of the devices. These demonstrations with the detector length of approximately 500 µm and a diameter of only 125 µm pave the way for miniaturized and high-performance implementations of our detector in a wide range of minimally invasive applications, especially intravascular and endoscopic.

1 | Introduction

Ultrasound detectors (UDs) play a vital role in many applications, such as biomedical imaging [1] and non-destructive testing [2]. Recently, UD development has been geared toward adaptation in space-constrained working environments such as endoscopic imaging [3–5], intravascular imaging [6] or in multimodal optical-optoacoustic microscopy [7]. In those implementations, it is critical to miniaturize the UDs without degrading their performance, i.e., their detection sensitivity and bandwidth [8]. A high sensitivity enhances the detection limit of the system by increasing the signal-to-noise ratio (SNR) while retaining the excitation fluence under medical approval thresholds, and a broad detection bandwidth reduces temporal and spatial uncertainties in the measurement, thus improving the achieved spatial resolutions [9]. A prominent example is the diagnosis of atherosclerosis associated with coronary artery disease, which requires the UD size of well under millimeter scale to fit into a conventional intravascular sheath, and the detection bandwidth of 100 MHz to accurately resolve the fibrous cap thickness, which is a hallmark of plaque stability [10]. Commonly used state of the art intervascular-ultrasound (IVUS) has limited ability to characterize the fibrous cap thickness [11], typically on the order of 50 µm, because the sensitivity of piezoelectric

transducers (PZTs) decreases quadratically with size, preventing PZTs miniaturization beyond the millimeter scale [12]. Therefore, commercial IVUS systems offer resolutions of only 40–50 μm [13], which prohibit accurate measurement of the fibrous cap thickness.

UDs based on microscale optical resonators (microresonators) have been proposed as alternatives to PZTs in applications that necessitate miniaturization [14]. The sensitivity with regard to miniaturizability, measured by per-area noise-equivalent pressure density (NEPD), of microresonator-based UDs was reported to be several orders of magnitude better than that of PZTs [14]. Unfortunately, achieving simultaneously high sensitivity and large bandwidth in a miniaturized microresonator-based UDs is not a trivial task. The most sensitive microresonator-based UDs employed acoustic membranes to exploit strong optomechanic coupling, which limits the detection bandwidth to several MHz around the resonant frequencies of the mechanical resonators [15, 16]. For Fabry-Perot resonators, increasing the bandwidth facilitates reducing the cavity thickness, which inherently degrades the sensitivity of the UDs [17]. UDs based on thin photonics waveguides, i.e., polymer micro-ring resonators and silicon pi-shifted Bragg grating, seem to be exempted from the sensitivity-bandwidth trade-off because of the strong confinement of light in the sub-wavelength cross-sections [18–21]. However, this method is associated with complex microfabrication routines that are available only at high-end fabrication institutions. In addition, the small cross-section of these photonics waveguides appears to be a double-edged sword, as on one hand, a small cross-section enables a large detection bandwidth, but on the other hand, it necessitates advanced packaging for interrogation of the microresonators using external laser sources [22]. Those packaging strategies—originally developed for optical communication or encapsulated stationary devices in data centers [23] – lack both the miniaturization and reliability required to operate in demanding biomedical applications such as intravascular imaging. To the best of our knowledge, there is no existing microresonator-based UD with an overall footprint of less than 1 mm that simultaneously supports high sensitivity (i.e., NEPD of <1 mPa/$\sqrt{\text{Hz}}$) and a broad bandwidth (i.e., 100 MHz), both of which are achievable by bulky PZTs (see Section S1). Thus, microresonator-based UDs still lag behind PZTs despite the apparent appeal to intravascular or endoscopic applications.

We have recently demonstrated a sensitive UD based on rigid silica microresonators over an ultra-broad bandwidth (160 MHz), owing to the enhanced interaction between light and ultrasound within the distance of several acoustic wavelengths from the detection aperture [24]. However, the light-ultrasound interaction of the reported UD cannot be enhanced without sacrificing the Q-factor, limiting the overall sensitivity to approximately 3 mPa/$\sqrt{\text{Hz}}$ in NEPD. We hypothesize that by decoupling the light-ultrasound interaction from the Q-factor of a microresonator-based UD, the overall sensitivity of the UD could be further enhanced without loss of bandwidth.

Here, we present the most sensitive microresonator-based UDs to date with an overall NEPD as low as <0.5 mPa/$\sqrt{\text{Hz}}$, a detection bandwidth of approximately 100 MHz, and a diameter of ϕ125 μm. We achieved this by increasing the interaction between the ultrasonic field and the optical field, which is confined in the cavity of the pi-shifted Fiber Bragg grating (pFBG) resonator. Using an OptA-based visualization and optical simulation, we were able to control the relative position of the confined optical field with respect to the ultrasound collecting aperture at resolutions of a few micrometers, maximizing light-ultrasound interaction without altering optical confinement. We show comparable performance of our new optical resonator-based UD, which we have named the D-shaped Fiber Bragg grating (DFBG), to state-of-the-art PZTs employed in pre-clinical OptA systems, despite the aperture of the DFBG being three orders of magnitude smaller in size. Finally, using the DFBG, we demonstrate the ability to detect OptA signals emitted from a single cell-sized absorber, which is commonly employed as an imaging phantom [25, 26], with an SNR of ~17 and without signal averaging at an exposure level less than 20% of the safety limit prescribed by the American National Standards Institute (ANSI).

2 | Results

Figure 1a illustrates the structure of the DFBG, which features a pi-shifted optical cavity sandwiched between two Bragg reflectors in the core of an optical fiber. We exposed this cavity to the detector's aperture by partially removing the cladding of a pi-shifted Fiber Bragg grating (pFBG). Removing the cladding enabled incident ultrasonic waves to hit the detection aperture, causing the physical dimensions and refractive index of the proximal cavity to be strongly perturbed. This is different from normal pFBGs, wherein the core region is buried deep inside the fiber. The large acoustic impedance mismatch between the glass cladding and water results in only a small fraction of the incident ultrasonic energy being transmitted from the outer media into the core of the pFBG, therefore only a small fraction of the ultrasound wave perturbs the core region [27]. Ultrasound-induced perturbation was read out by interrogation of a continuous wave laser whose emission wavelength corresponded to the maximum slope of the resonant dip (see Method section "Detector interrogation").

To fabricate the DFBG, a pFBG was glued to a metallic fiber holder using ultraviolet (UV) curable epoxy (Figure 1b) so that the pFBG was bent along the curved surface of the holder. The cladding of the pFBG was partially removed by polishing the curved surface of the holder with diamond lapping film, resulting in a pFBG with a D-shaped cross section and a remaining thickness h (Figure 1c) (see Method section "Cladding removal"). The fiber cladding at the apex of the curved surface is removed the most compared to the cladding of the proximal region. Thus, it was necessary to align the invisible pi-shifted cavity to the apex of the curvature in order to bring the ultrasound collecting aperture as close as possible to the confined light. We achieved this by aligning two physical markers: a groove on the fiber holder at the apex of the curved surface, and a second marker on the outer cladding of the pFBG at the position of the pi-shifted cavity (see Figure 1a).

To make the second marker, we first located the pi-shifted cavity using a method called optoacoustic mapping of optical distribution (OMOD) (see Method section "Optoacoustic Mapping of Optical Distribution"). Figure 1d depicts the OMOD setup, wherein the pFBG was scanned over an ultrasonic point source generated by tightly focusing a nanosecond pulsed laser beam onto a thin gold film. The OMOD method mapped the

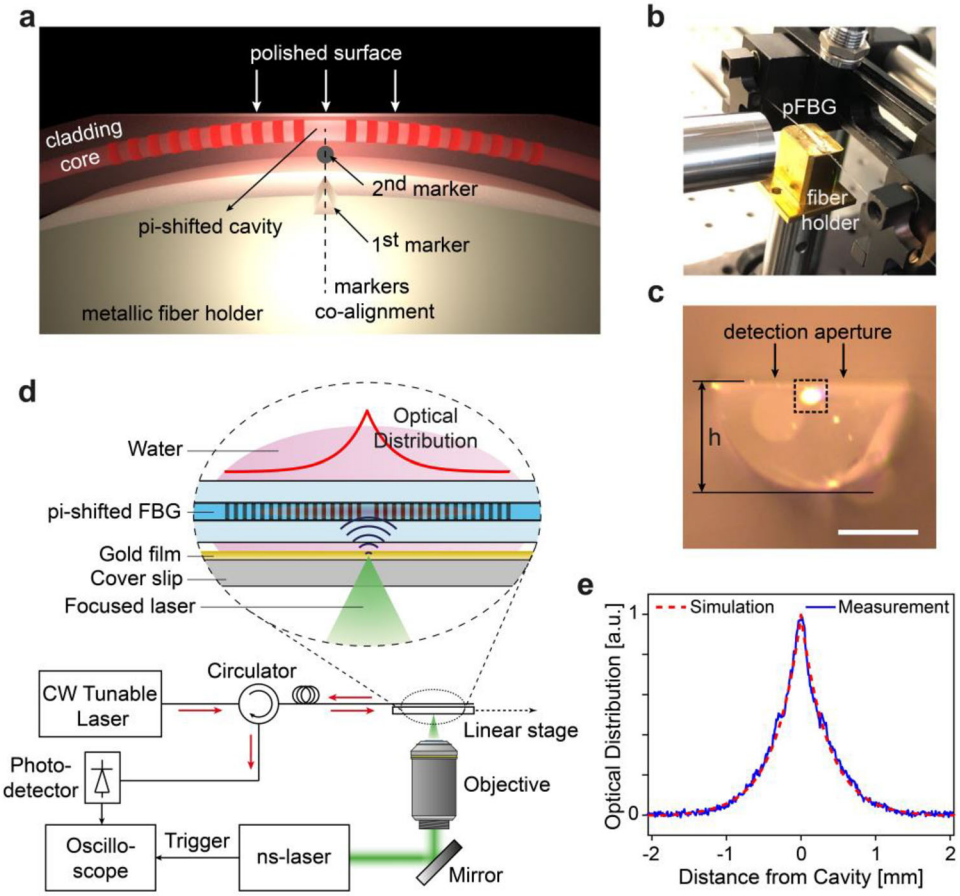

FIGURE 1 | Structure and fabrication of the D-shaped Fiber Bragg grating (DFBG). (a) Schematic illustration of the DFBG, which was created by partially removing the cladding of a pi-shifted Fiber Bragg grating (pFBG) and leaving the pi-shifted cavity exposed to the detection aperture. It is critical to place the pi-shifted cavity at the center of the fiber holder via co-alignment of two markers that indicate the correct position on the holder (first marker) and on the fiber (second marker). (b) A photograph of the pFBG, which is immobilized onto the holder prior to fabrication of the DFBG. (c) An image showing the D-shaped cross-section of the DFBG with a remained thickness h of 70 μm. The center of the fiber is marked with a dashed square. The core region is interrogated with white light for visualization. (d) A schematic illustration of the optoacoustic mapping of optical distribution (OMOD) setup used to precisely determine the position of the pi-shifted cavity and create the second marker. (e) Simulated optical distribution inside the pFBG compared to the measured distribution using the OMOD setup.

sensitivity distribution of the pFBG, representing the local optical intensity [28]. Figure 1e highlights the excellent match between measurements of the optical distribution of the pFBG using the OMOD method and a simulated theoretical distribution. The location of the pi-shifted cavity at the point of maximum optical distribution was visually marked (see Method section "Cavity marking") and aligned on top of the first marker under a microscope.

In order to quantify the effect of light-ultrasound interaction on the sensitivity of the detector, we measured the relative sensitivity of the DFBG as a function of the distance between the aperture and the center of the pFBG core—which is represented by the remained thickness h of the fiber (Figure 2a). The sensitivity shows a five-fold improvement as h decreased from 125 μm to 75 μm while the Q-factor remained unchanged (decoupling regime). This finding suggests that the change in sensitivity of the DFBG was solely the result of stronger light-ultrasound interaction (see Section S2) as opposed to sensitivity gain that results in a sacrifice of the Q-factor due to degradation of the optical confinement when bringing the aperture closer to the center of the pFBG core [24]. As both the distance to the aperture and the Q-factor contribute to the sensitivity, the method presented in this work results in superior sensitivity. When h decreased below 75 μm, the Q-factor drops significantly and the sensitivity collapses (lossy regime).

Figure 2b presents a simulation of the optical confinement inside the DFBG, elaborating on the relationship between Q-factor and h observed in Figure 2a. When h decreased from 125 μm to 75 μm, the DFBG experienced negligible effects from the polishing process, and the Q-factor remained stationary. As h decreased to approximately 65 μm, the guided mode became distorted in profile and experienced noticeable energy loss because the aperture alters the guiding condition and induces substantial propagation losses. This results in a sharp drop in the Q-factor (see Section S3). At $h < 63$ μm, the optical fiber supports only leaky modes. Therefore, the optical energy is no longer confined in the cavity, and the resonant behavior of the DFBG disappears.

Figure 2c,d displays OptA microscope (OAM) images of a knotted suture phantom under the same optical excitation using two dif-

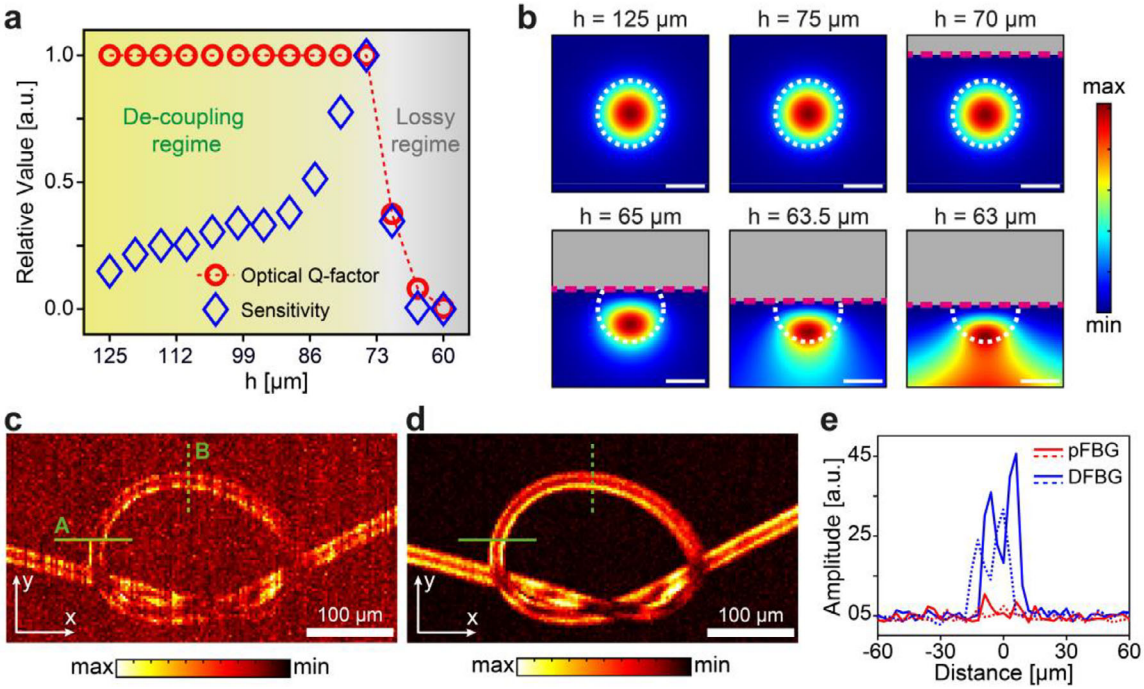

FIGURE 2 | Sensitivity enhancement of the D-shaped Fiber Bragg Grating (DFBG) due to increased light-ultrasound interaction. (a) Sensitivity and optical Q-factor of the DFBG with respect to the remaining thickness (h). (b) Mode distribution inside the D-shaped fiber at different values of h. All sub-figures show the optical intensity of the guided mode of the DFBG within a 20 x 20 μm region around the center of the fiber (the region marked with a dashed square in Figure 1c). The white scale bar corresponds to 5 μm. The white dashed circle represents the boundary between the core (inner region) and the cladding (outer region) of the fiber. The pink dashed line represents the detection aperture. The space above the detection aperture is filled with water (light grey). (c, d) Optoacoustic (OptA) microscope images of a knotted suture using a pi-shifted Fiber Bragg Grating (pFBG) (c) and the DFBG (d) as the OptA detector under the same excitation. (e) A comparison of intensity profiles from two different locations on the microscope images in Figure 2c,d. Solid and dashed profile lines correspond to the solid (A-line) and dashed (B-line) lines in Figure 2c,d, respectively.

ferent OptA detectors, an original pFBG detector with h = 125 μm (Figure 2c) and the DFBG detector with h = 75 μm (Figure 2d), to visualize the effect of enhanced light-ultrasound interaction on image quality (see Method section "Suture microscopy"). The laser energy was set at approximately 75 nJ/pulse—which is several orders of magnitude smaller than the energy used in other optical-sensor-based microscopy [7, 29]. Figure 2e presents intensity profiles from both OptA microscope images, showing that the improved sensitivity of the DFBG resulted in a clearly observable enhancement in OptA image contrast.

Figure 3 illustrates a side-by-side comparison between the DFBG and two state-of-the-art focused PZTs transducers employed in commercial OptA mesoscopy systems, namely fPZT25 and fPZT50 (see Section S4). Figure 3a depicts the spectral response of the three detectors. The DFBG demonstrates a broader bandwidth and a higher center frequency than the two PZTs, but also a non-uniform frequency response, which is typical of fiber-based UDs [29, 30]. The gaps in the DFBG's bandwidth (around 50 MHz and a second harmonic around 100 MHz) correspond to the reverberation of acoustic waves within the fiber, because the large acoustic impedance mismatch between silica and water/acoustic gel creates an acoustic resonator [31]. The exact location of the spectral gap is governed by the dimension of the fiber itself. In our case, the locations of the major dips correspond to the longitudinal reverberation across the whole remained thickness (h = 75 um) of the silica fiber. This effect can be mitigated by deposition of matching layers at the back side of the DFBG opposite to the aperture [32]. Nevertheless, this broad bandwidth enables axial resolution of 6.5 (for resolution characterization see Section S5)—which is at least 7-folds finer than that of a state-of-the-art IVUS [13].

Figure 3b shows the amplitude of the recorded OptA signals from all three detectors with respect to the distance between the OptA source and the detection apertures. The OptA signal was created by focusing a nanosecond laser onto a black vinyl film, which emitted the OptA signal in the frequency range of 10–30 MHz. The amplitude of the OptA signal from the DFBG (blue dashed curve) followed the amplitude of a spreading spherical wave, i.e., inversely proportional to the distance, suggesting that the sensitivity of the DFBG was independent of the distance between the detector and the source. In contrast, the signal amplitudes of the two focused PZTs (red and orange dashed curves) strongly depended on the source-to-detector distance due to the acoustic focusing [1] and reached the maximal values at distances corresponding to their focal length. At the focal distances, the overall NEPDs of the two focused PZTs were characterized to be 0.35 and 0.40 mPa/$\sqrt{\text{Hz}}$ for the fPZT25 and fPZT50, respectively, over a 20-MHz bandwidth around their center frequencies. The overall NEPD of the DFBG was characterized to be 0.42 mPa/$\sqrt{\text{Hz}}$ over the same bandwidth (see Method section "Sensitivity characterization" and Section S6). However, our results show that the DFBG has a more robust sensitivity response, as the sensitivity of the two focused PZTs falls very quickly below the sensitivity of the DFBG when the

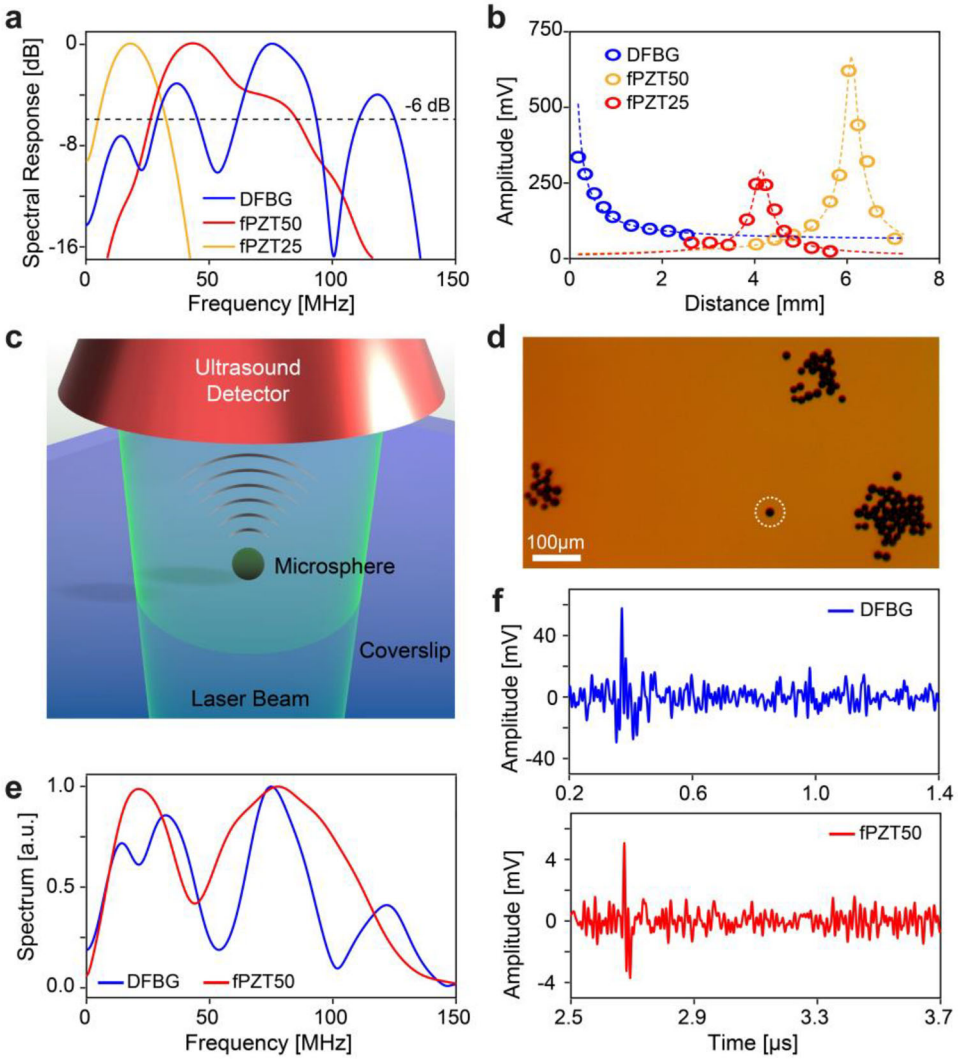

FIGURE 3 | Comparison of the D-shaped Fiber Bragg Grating (DFBG) and two focused piezoelectric transducers (PZTs). (a) Frequency response of all three detectors. The -6 dB bandwidths of the three detectors are approximately 30 MHz, 80 MHz, and 100 MHz for the fPZT25, fPZT50, and DFBG, respectively. (b) Optoacoustic (OptA) signals measured by all three detectors from the same OptA point source as a function of the distance between the source and the detector. All signals were normalized to the background. Corresponding fits are depicted by dashed lines. (c) Illustration of the single-particle sensing experiment, where a black microsphere immobilized on a cover slip using transparent adhesive is irradiated by a loosely-focused nanosecond laser beam, and the emitted OptA signal is detected by an ultrasound detector (UD). (d) A microscope image of the coverslip used in the single-particle sensing experiment. The dashed white circle contains the microsphere selected for analysis. (e) Spectra of the two OptA signals recorded from the microsphere using the DFBG (blue) and the fPZT50 (red) as the UD during the experiment depicted in Figure 3c. Differences between these spectra result from differences in the frequency response of the two UDs used to record the OptA signals (Figure 3a). (f) Time-domain OptA signals recorded using the DFBG (blue) and the fPZT50 (red).

acoustic source is located outside of the focal plane, even by a small distance (~150 µm for the fPZT25, ~60 µm for the fPZT50).

Next, we compared the OptA sensing performance of the DFBG and the fPZT50, which was chosen for comparison due to having the most similar frequency response to the DFBG (Figure 3a). Figure 3c illustrates the experiment setup, wherein a polystyrene microsphere with a diameter of approximately 15 µm was illuminated by a loosely-focused laser beam (see Method section "Single microsphere sensing"). Figure 3d depicts a microscope image of the cover slip used for this experiment. To ensure that the recorded OptA signals were emitted from a single microsphere, we chose an isolated microsphere (enclosed by a dashed circle) and illuminated it with a laser beam with a diameter of approximately 60 µm to avoid co-illumination of nearby microspheres. The OptA signal emitted from the microsphere was recorded by the DFBG at a distance of 0.5 mm and by the fPZT50 at its optimal (focal) distance. Figure 3e shows the spectra of the OptA signals captured by the two detectors, confirming that the recorded OptA signals originated from a single microsphere. Both spectra have a noticeable dip at ~45 MHz, which is attributed to the destructive interference between the OptA signal reflected at the interface of the adhesive layer and the cover slip and the OptA signal propagating directly toward the detector (see Section S7). The spectrum of the signal obtained by the DFBG showed additional dips that reflect the dips in the frequency response

of the DFBG (Figure 3a). The time-domain signal-to-noise ratios (SNR) without signal averaging were 17 for the DFBG and 17.9 for the fPZT50 (Figure 3f).

3 | Discussion

In this work, we constructed one of the most sensitive optical-resonator-based UDs to date by successfully decoupling the light-ultrasound interaction from the Q-factor of the resonator. The sensitivity, bandwidth, and imaging performance of the DFBG are demonstrated to be comparable to state-of-the-art focused PZTs that are hundreds of times larger than the DFBG. The high bandwidth of the DFBG is also shown to enable axial resolution of 6.5 um, which is very attractive for intravascular applications like characterizing the fibrous cap thickness that is associated with coronary artery disease, surpassing the state-of-the-art IVUS by ~7-fold.

While the sensitivity of focused PZTs depends on their working distance, the sensitivity of the DFBG is generally independent of the working distance. This characteristic could favor the DFBG in OAM because typical systems employing focused PZTs must defocus the PZT so that the acoustic detection field of the focused PZT covers the microscope field-of-view [33]. This defocusing forces PZTs to operate outside of their optimal working distances and reduces the sensitivity of the system by several fold.

In addition, the distance-independent sensitivity and the microscale dimension of the DFBG would enable easy and seamless integration of OptA contrast into intravascular catheters and endoscopes, as well as any conventional optical microscope. Furthermore, the overall NEPD of the DFBG can be further enhanced with advanced low noise interrogation systems, such as pulse interferometry [34], phase detection [35] or balanced detection [36, 37] (see Section S8 for detailed explanation).

Using the DFBG, we also demonstrated OAM and OptA sensing using low laser energy, with conditions that are easily achievable by over-driving continuous wave (CW) laser diodes [38]. The excitation pulse energy in the microsphere sensing experiment was roughly 75 nJ/pulse, while the OAM experiment used an excitation pulse energy of 120 nJ/pulse, and a typical CW laser diode can emit pulse energy up to >200 nJ/pulse [38]. Previously demonstrated OptA systems, which employ optical-resonator-based UDs, often use excitation energies two to three orders of magnitude higher than the energy used here, which can only be accomplished by using expensive and bulky Q-switch lasers [7, 29]. Integrating laser diodes would significantly reduce the complexity and increase the affordability of potential OptA systems. Furthermore, laser diodes offer high repetition rates at hundreds of kHz, which enable the acquisition of large numbers of measurements and the averaging of thousands of signals while still maintaining video-rate sensing or imaging (tens of Hz). This would further improve SNR and enable fast imaging in clinical volatile environmental conditions.

We have presented a sensitive and miniaturized UD using an innovative method that does not require complex micro-fabrication facilities. By accurate removal of the fiber cladding, the enhanced interaction between the confined light field and the outer ultrasound field facilitates a boost in sensitivity. However, the mechanical strength of the fiber is reduced as a consequence of the cladding removal, necessitating gentle handling or proper mechanical protection. Improving the mechanical stability would require the use of guiding sheaths, which are common in intervascular and endoscopic applications [6, 39], and filling the polished area with polymers or UV-curable epoxies that improve the acoustic impedance matching and mechanical durability of the sensor.

In addition, it is worth mentioning that the current DFBG was optimized for operation in water. For other operational environments, i.e., air-coupled ultrasound sensing, the guided mode behaves differently, so additional analysis is required to find the optimized configuration. Nevertheless, our proposed DFBG detector, which is embedded inside a conventional optical fiber, has essentially solved the sensitivity versus miniaturization problem associated with both mature PZT technology and microresonator-based detectors, and thus could facilitate advancements in miniaturized and minimally invasive OptA imaging systems.

4 | Methods

4.1 | Optoacoustic Mapping of Optical Distribution (OMOD)

To visualize the optical intensity distribution inside a pFBG (TeraXion, Canada), we scanned the pFBG over an OptA point source created by focusing a nanosecond laser (Flare PQ H GR 2k-500, Innolight, Germany) onto a 200-nm-thick gold layer coated on a cover slip. A microscope objective (PLN 10x—NA = 0.25, Olympus) was then used to create a spot size of less than 5 μm in diameter. The pFBG was immobilized on a high-precision scanning stage (MLS203-1, Thorlabs, USA), parallel to and almost touching the gold-coated surface. The space between the gold-coated surface and the pFBG was filled with water for ultrasound coupling. The pFBG was scanned with a step size of 2 μm with the scan direction parallel to the axial direction of the pFBG. At each scanning point, the peak-to-peak amplitudes of the OptA signal emitted from the point source were recorded. Those peak-to-peak amplitudes were directly proportional to the intensity of the optical field inside the pFBG at the position above the OptA point source [28] and were plotted in Figure 1e.

4.2 | Cavity Marking

While preparing to create the DFBG, we created a visual marker on a pFBG at the position of the pi-shifted cavity to facilitate alignment of this cavity with the fiber holder. After measurement with the OMOD method, the pFBG was moved using the scanning stage to the position where the pFBG reached its maximum sensitivity, ensuring that the pi-shifted cavity was at the position of the OptA point source (illustrated by the inset in Figure 1d). Then, the coupling water was drained, and the gold-coated cover slip was carefully removed so as not to touch the pFBG. Next, we slightly lifted the microscope objective to focus the laser beam onto the surface of the pFBG and increased the laser power. Under

sufficient laser power and after enough time (approximately 10–15 s), the focused laser beam burned a dark spot onto the surface of the pFBG with a diameter not larger than that of the focal spot (<5 μm). This burned spot served as the cavity marker for alignment of the pFBG onto the fiber holder.

4.3 | Cladding Removal

To create the DFBG, we fixed the pFBG onto a custom metallic holder designed to have a flat bottom surface and a curved top surface with a radius of curvature of 5 cm. We fabricated a marker using a high-precision computer numeric control (CNC) machine and used it to mark the apex position of the curved top surface. A V-groove running across the direction of the curve was used to hold the pFBG. We used a microscope to carefully align the pFBG onto the V-groove so that the cavity marker on the pFBG aligned with the marker on the holder. This step ensured maximum exposure of the pi-shifted cavity to the polished detection aperture. Then, UV curable epoxy (NOA 81, Norland, USA) was dropped along the V-groove and cured to firmly fix the pFBG onto the holder. The holder was then inserted into a custom metallic polishing disk and polished with diamond lapping films (LF1D and LFCF, Thorlabs, USA) to partially remove the fiber cladding, forming the DFBG. Once finished, the DFBG was removed from the metallic holder by heating the holder to approximately 200°C. The high temperature softened the epoxy glue used to fix the DFBG, allowing the DFBG to be lifted from the holder. The residual epoxy on the surface of the DFBG was removed by soaking the DFBG in methylene chloride (CH_2Cl_2, Sigma Aldrich, USA).

4.4 | Detector Interrogation

To measure ultrasound signals, the DFBG detector was interrogated by a tunable CW laser (ITUNX 1550B, Thorlabs Inc., USA) that emits laser light at a wavelength of approximately 1549 nm and at an output power of approximately 10 dBm. The reflected optical output from the detector was then directed to a balanced photodetector (PDB480C-AC, Thorlabs Inc., USA) by an optical circulator (CTR1550PM-APC, Thorlabs Inc., USA). The high-frequency (30 kHz–1.5 GHz) output of the photodetector, which contains collected ultrasound data, was digitized using a high-speed data acquisition card (CSE123G2, GaGe, USA). The same method was used to interrogate a pFBG when it was used as an OptA detector [27].

4.5 | Suture Microscopy

To test the image contrast afforded by the DFBG during OR-OAM, we prepared a suture phantom by tying a black suture (Dafilon Polyamide, B. Braun Melsungen) with a diameter in the range of 10–19 μm into the shape of a knot. A layer of optically clear adhesive tape (OCA8146-2, Thorlabs, USA) was applied onto the surface of a cover slip. The knotted suture was then placed on top of the adhesive tape for immobilization. The same ns-laser and microscope objective as described in the Method section "Optoacoustic mapping of optical distribution" were used for optical excitation. The DFBG and pFBG detectors were placed 0.5 mm away from the knotted suture, and the space between the phantom and the detectors was filled with distilled water for ultrasound coupling.

The suture phantoms were fixed on top of a high-precision microscopic stage (MLS203-1, Thorlabs Inc., USA) and raster-scanned with a step size of 3 μm in both X and Y directions. The excitation pulse energy of the laser was 120 nJ/pulse, and the laser repetition rate was 1.35 kHz. At each position, the OptA signal was recorded once. The OR-OAM image was plotted by mapping the maximum intensity projection of the recorded OptA signals.

4.6 | Sensitivity Characterization

To characterize the sensitivity of the OptA detectors, we calibrated their response with a reference needle hydrophone (0.5-mm diameter, Precision Acoustics, UK) in the frequency range from 10 MHz to 30 MHz. The OptA source for calibration was generated by focusing the ns-laser pulse onto a black vinyl film with water as the coupling medium. The pulse energy for OptA excitation was set at 230 nJ/pulse, and the responses of the OptA detectors were recorded without signal averaging.

4.7 | Single Microsphere Sensing

To prepare the sample for the microsphere sensing experiment, we first put a layer of optically clear adhesive tape (OCA8146-2, Thorlabs, USA) onto the surface of a cover slip. Polystyrene microspheres with diameters ranging from 10 μm to 20 μm were dropped onto the adhesive tape layer. The polyester release liner of the tape was used to gently press the microspheres onto the tape to ensure good adhesion. We used a microscope to locate an isolated microsphere with no nearby neighbors and illuminated the microsphere with an ns-laser beam focused through a microscope objective. The objective was defocused, so the diameter of the beam was approximately 60 μm, which is sufficient to cover the whole microsphere. The laser energy was 74 nJ/pulse, and the repetition rate of the laser was 1.35 kHz, which corresponds to an energy exposure of 2.6 mJ/cm^2 and an optical power exposure of 3.5 W/cm^2. These exposure levels are less than 20% of the ANSI safety limit for visible radiation (20 mJ/cm^2 and 18 W/cm^2) [40].

Author Contributions

T.L. and R.S. conceived the idea of the detector. T.L., R.S., and V.N. wrote the paper. T.L. fabricated the detectors, performed the experiments, and analyzed the data. V.N. provided the funding.

Acknowledgements

V.N. acknowledges financial support from the European Union's Horizon 2020 programme under Grant Agreement No. 862811 (RSENSE) and from the European Research Council (ERC) No. 694968 (PREMSOT), from the DZHK (German Centre for Cardiovascular Research; FKZ 81Z0600104), and from the Deutsche Forschungsgemeinschaft (DFG), Germany [Gottfried Wilhelm Leibniz Prize 2013; NT 3/10-1 and as part of the CRC 1123 (Z1)]. We thank Dr. Elisa Bonnin and Dr. Serene Lee for their comments and editing of this manuscript.

Open access funding enabled and organized by Projekt DEAL.

Conflicts of Interest

V.N. is a founder and equity owner of Maurus OY, Thesis GmbH, iThera Medical GmbH, Spear UG, and I3 Inc. The remaining authors declare no competing interests.

Data Availability Statement

All the data supporting this study have been provided in this manuscript and its supplement information.

References

1. R. S. C. Cobbold, *Foundations of Biomedical Ultrasound*, Oxford University Press, Oxford, 2007.

2. C. A. C. L. Sourav Banerjee, *Computational Nondestructive Evaluation Handbook: Ultrasound Modeling Techniques*, CRC Press, Boca Raton, 2020, https://doi.org/10.1201/9780429456909.

3. Y. Liang, W. Fu, Q. Li, et al., "Optical-Resolution Functional Gastrointestinal Photoacoustic Endoscopy Based on Optical Heterodyne Detection of Ultrasound," *Nature Communications* 13 (2022): 7604, https://doi.org/10.1038/s41467-022-35259-5.

4. J.-M. Yang, C. Favazza, R. Chen, et al., "Simultaneous Functional Photoacoustic and Ultrasonic Endoscopy of Internal Organs In Vivo," *Nature Medicine* 18 (2012): 1297–1302, https://doi.org/10.1038/nm.2823.

5. J. Kim, D. Heo, S. Cho, et al., "Enhanced Dual-Mode Imaging: Superior Photoacoustic and Ultrasound Endoscopy in Live Pigs Using a Transparent Ultrasound Transducer," *Science Advances* 10 (2024): adq9960, https://doi.org/10.1126/sciadv.adq9960.

6. J. Wang, Z. Zheng, J. Chan, and J. T. W. Yeow, "Capacitive Micromachined Ultrasound Transducers for Intravascular Ultrasound Imaging," *Microsystems & Nanoengineering* 6 (2020): 73, https://doi.org/10.1038/s41378-020-0181-z.

7. R. Shnaiderman, G. Wissmeyer, M. Seeger, et al., "Fiber Interferometer for Hybrid Optical and Optoacoustic Intravital Microscopy," *Optica* (2017): 4, https://doi.org/10.1364/optica.4.001180.

8. C. Moore and J. V. Jokerst, "Strategies for Image-Guided Therapy, Surgery, and Drug Delivery Using Photoacoustic Imaging," *Theranostics* 9 (2019): 1550–1571, https://doi.org/10.7150/thno.32362.

9. P. Beard, "Biomedical Photoacoustic Imaging," *Interface Focus* 1 (2011): 602–631, https://doi.org/10.1098/rsfs.2011.0028.

10. A. P. Burke, A. Farb, G. T. Malcom, Y.-H. Liang, J. Smialek, and R. Virmani, "Coronary Risk Factors and Plaque Morphology in Men With Coronary Disease Who Died Suddenly," *New England Journal of Medicine* 336 (1997): 1276–1282, https://doi.org/10.1056/nejm199705013361802.

11. L. Räber and Y. Ueki, "Optical Coherence Tomography- vs. Intravascular Ultrasound-Guided Percutaneous Coronary Intervention," *Journal of Thoracic Disease* 9 (2017): 1403.

12. A. M. Winkler, K. Maslov, and L. V. Wang, "Noise-Equivalent Sensitivity of Photoacoustics," *Journal of Biomedical Optics* 18 (2013): 097003, https://doi.org/10.1117/1.Jbo.18.9.097003.

13. A. Vasquez, N. Mistry, and J. Singh, "Impact of Intravascular Ultrasound in Clinical Practice," *Interventional Cardiology Review* 9, no. 3 (2014): 156–163, https://doi.org/10.15420/icr.2014.9.3.156.

14. G. Wissmeyer, M. A. Pleitez, A. Rosenthal, and V. Ntziachristos, "Looking at Sound: Optoacoustics with All-Optical Ultrasound Detection," *Light: Science & Applications* 7 (2018): 53, https://doi.org/10.1038/s41377-018-0036-7.

15. W. J. Westerveld, M. Mahmud-Ul-Hasan, R. Shnaiderma, et al., "Sensitive, Small, Broadband and Scalable Optomechanical Ultrasound Sensor in Silicon Photonics," *Nature Photonics* 15 (2021): 341–345, https://doi.org/10.1038/s41566-021-00776-0.

16. S. M. Leinders, W. J. Westerveld, J. Pozo, et al., "A Sensitive Optical Micro-Machined Ultrasound Sensor (Omus) Based on a Silicon Photonic Ring Resonator on an Acoustical Membrane," *Scientific Reports* 5 (2015): 14328, https://doi.org/10.1038/srep14328.

17. J. A. Guggenheim, J. Li, T. J. Allen, et al., "Ultrasensitive Plano-Concave Optical Microresonators for Ultrasound Sensing," *Nature Photonics* 11 (2017): 714–719, https://doi.org/10.1038/s41566-017-0-027-x.

18. Y. Hazan, A. Levi, M. Nagli, and A. Rosenthal, "Silicon-Photonics Acoustic Detector for Optoacoustic Micro-Tomography," *Nature Communications* 13 (2022): 1488, https://doi.org/10.1038/s41467-022-29179-7.

19. J. Pan, Q. Li, Y. Feng, et al., "Parallel Interrogation of the Chalcogenide-Based Micro-Ring Sensor Array for Photoacoustic Tomography," *Nature Communications* 14 (2023): 3250, https://doi.org/10.1038/s41467-023-39075-3.

20. M. Nagli, R. Moisseev, N. Suleymanov, et al., "Silicon Photonic Acoustic Detector (Spade) Using a Silicon Nitride Microring Resonator," *Photoacoustics* (2023): 32, https://doi.org/10.1016/j.pacs.2023.100527.

21. R. Shnaiderman, G. Wissmeyer, O. Ülgen, Q. Mustafa, A. Chmyrov, and V. Ntziachristos, "A Submicrometre Silicon-On-Insulator Resonator for Ultrasound Detection," *Nature* 585 (2020): 372–378, https://doi.org/10.1038/s41586-020-2685-y.

22. R. Marchetti, C. Lacava, L. Carroll, K. Gradkowski, and P. Minzioni, "Coupling Strategies for Silicon Photonics Integrated Chips," *Photonics Research* 7 (2019): 201–239, https://doi.org/10.1364/prj.7.000201.

23. L. Carroll, J. S. Lee, C. Scarcella, et al., "Photonic Packaging: Transforming Silicon Photonic Integrated Circuits Into Photonic Devices," *Applied Sciences* 6 (2016): 426, https://doi.org/10.3390/app6120426.

24. T. A. La, O. Ülgen, R. Shnaiderman, and V. Ntziachristos, "Bragg Grating Etalon-Based Optical Fiber for Ultrasound and Optoacoustic Detection," *Nature Communications* 15 (2024): 7521, https://doi.org/10.1038/s41467-024-51497-1.

25. M. Omar, D. Soliman, J. Gateau, and V. Ntziachristos, "Ultrawideband Reflection-Mode Optoacoustic Mesoscopy," *Optics Letters* 39 (2014): 3911–3914, https://doi.org/10.1364/ol.39.003911.

26. M. Omar, J. Gateau, and V. Ntziachristos, "Raster-Scan Optoacoustic Mesoscopy in the 25–125 Mhz Range," *Optics Letters* 38 (2013): 2472–2474, https://doi.org/10.1364/ol.38.002472.

27. A. Rosenthal, D. Razansky, and V. Ntziachristos, "High-Sensitivity Compact Ultrasonic Detector Based on a Pi-Phase-Shifted Fiber Bragg Grating," *Optics Letters* 36 (2011): 1833–1835, https://doi.org/10.1364/OL.36.001833.

28. M. Á. A. C. Amir Rosenthal, S. Kellnberger, D. Razansky, and V. Ntziachristos, "Spatial Characterization of the Response of a Silica Optical Fiber to Wideband Ultrasound," *Optics Letters* 37 (2012): 3174–3176, https://doi.org/10.1364/OL.37.003174.

29. G. Wissmeyer, D. Soliman, R. Shnaiderman, A. Rosenthal, and V. Ntziachristos, "All-Optical Optoacoustic Microscope Based on Wideband Pulse Interferometry," *Optics Letters* 41 (2016): 1953–1956, https://doi.org/10.1364/ol.41.001953.

30. D. R. Amir Rosenthal and V. Ntziachristos, "High-Sensitivity Compact Ultrasonic Detector Based on a Pi-Phase-Shifted Fiber Bragg Grating," *Optics Letters* 36 (2011): 1833–1835, https://doi.org/10.1364/OL.36.001833.

31. T. Berer, I. A. Veres, H. Grün, J. Bauer-Marschallinger, K. Felbermayer, and P. Burgholzer, "Characterization of Broadband Fiber Optic Line Detectors for Photoacoustic Tomography," *Journal of Biophotonics* 5 (2012): 518–528, https://doi.org/10.1002/jbio.201100110.

32. L. Wang, Y. Zhao, B. Zheng, et al., "Ultrawide-Bandwidth High-Resolution All-Optical Intravascular Ultrasound Using Miniaturized Photoacoustic Transducer," *Science Advances* 9 (2023): adg8600, https://doi.org/10.1126/sciadv.adg8600.

33. S. Kellnberger, D. Soliman, G. J. Tserevelakis, et al., "Optoacoustic Microscopy at Multiple Discrete Frequencies," *Light: Science & Applications* 7 (2018): 109, https://doi.org/10.1038/s41377-018-0101-2.

34. A. Rosenthal, S. Kellnberger, D. Bozhko, et al., "Sensitive Interferometric Detection of Ultrasound for Minimally Invasive Clinical Imaging Applications," *Laser & Photonics Reviews* 8 (2014): 450–457, https://doi.org/10.1002/lpor.201300204.

35. L. Riobó, Y. Hazan, F. Veiras, M. Garea, P. Sorichetti, and A. Rosenthal, "Noise Reduction in Resonator-Based Ultrasound Sensors by Using a CW Laser and Phase Detection," *Optics Letters* 44 (2019): 2677–2680, https://doi.org/10.1364/ol.44.002677.

36. L. Hu, G. Liu, Y. Zhu, X. Luo, and M. Han, "Laser Frequency Noise Cancelation in a Phase-Shifted Fiber Bragg Grating Ultrasonic Sensor System Using a Reference Grating Channel," *IEEE Photonics Journal* 8 (2016): 1–8, https://doi.org/10.1109/jphot.2016.2527018.

37. Y. O. Qi Wu, "High-Sensitivity Ultrasonic Phase-Shifted Fiber Bragg Grating Balanced Sensing System," *OPTICS EXPRESS* 20 (2012): 28353–28362.

38. A. Stylogiannis, L. Prade, A. Buehler, J. Aguirre, G. Sergiadis, and V. Ntziachristos, "Continuous wave laser diodes enable fast optoacoustic imaging," *Photoacoustics* 9 (2018): 31–38, https://doi.org/10.1016/j.pacs.2017.12.002.

39. C. E. Munding, E. Chérin, I. Jourard, et al., "Development of a 3 French Dual-Frequency Intravascular Ultrasound Catheter," *Ultrasound in Medicine & Biology* 44 (2018): 251–266, https://doi.org/10.1016/j.ultrasmedbio.2017.09.015.

40. American National Standard for Safe Use of Lasers (ANSI Z136.1-2007, Laser Institute of America).

Supporting Information

Additional supporting information can be found online in the Supporting Information section.

Supporting file: lpor70702-sup-0001-SuppMat.docx